Rician Noise and Intensity Nonuniformity Correction (NNC) Model for MRI Data

Lu Liu[a], Huan Yang[a], Jiyun Fan[a,b], Ryan Wen Liu[c], Yuping Duan[a,*]

[a] *Center for Applied Mathematics, Tianjin University*
[b] *School of Mathematics and Statistics, Henan University*
[c] *School of Navigation, Wuhan University of Technology*

Abstract

Rician noise and intensity nonuniformity are two common artifacts and usually coexist in magnetic resonance imaging (MRI) data. Many methods have been proposed in the literature dealing with either Rician noise or intensity nonuniformity individually. We numerically verify that the existence of intensity nonuniformity may lead to the underestimation of noise, which means intensity nonuniformity influences the performance of denoising and vice versa. Thus, we propose a novel restoration model via a *Maximum a Posteriori (MAP) estimator* by regarding MRI data as a combination of two multiplicative components, namely, the true intensity and the bias field, and a noise followed a Rician distribution. We also guarantee that the proposed model has at least one positive nontrivial solution theoretically. An efficient algorithm based on alternating minimization method is developed, all subproblems of which can be solved effectively by either Newton's method or closed-form solutions. Intensive numerical results on synthetic and real MRI data confirm the robustness of the method and its better performance for MRI data restoration.

Keywords: Rician noise, Intensity nonuniformity, Total variation, Alternating minimization method, Primal-dual algorithm

*Corresponding author
Email address: yuping.duan@tju.edu.cn (Yuping Duan)

1. Introduction

Magnetic resonance images may be affected by several sources of degeneration during image acquisition and transmission, where Rician noise and intensity nonuniformity are two kinds of commonly seen artifacts in MRI data. Signal measured in MRI is a complex data and magnitude data is most common to avoid the the problem of phase artifacts [1]. In single-coil system, both real and imaginary part are corrupted by zero mean uncorrelated Gaussian noise with equal variance in the k-space domain, and the magnitude of the complex signal follows a stationary Rician distribution. Intensity nonuniformity is usually caused by a number of factors such as B1 and B0 field inhomogeneity, poor radiofrequency coil uniformity and patient dependent interactions. Although these are not serious problems for radiological quality diagnosis, they challenge the performance of the automated quantitative methods relying on the assumption of uniform intensity for the same tissue, such as registration and segmentation, etc. Thus, it is an important preprocessing step for the quantitative MRI data analysis to correct Rician noise and intensity nonuniformity.

According to the summarization of [2, 3] and the references contained therein, the image models for modeling the intensity nonuniformity can be classified into three categories depending on the relationship among the inhomogeneity-free image function $u(x)$, bias field function $b(x)$, and noise function $n(x)$. The most common model assumes the true intensity function is corrupted by small perturbation induced by the bias field function, and the noise arises from the scanner is independent of the bias field [4]

$$\text{Model I:} \qquad f(x) = u(x)b(x) + n(x). \tag{1}$$

The second image model keeps the hypothesis of biological noise, which is caused due to variations in tissue properties and modulated by the bias field [5, 6]

$$\text{Model II:} \qquad f(x) = (u(x) + n(x))b(x). \tag{2}$$

The third model comes from Model I, which applies the logarithmic transform to the MRI data to transfer the multiplicative bias field into additive effect in the log-space

[7, 8]. In this case, a biological noise is usually introduced in the log-space as

$$\text{Model III:} \quad \log f(x) = \log u(x) + \log b(x) + n(x). \tag{3}$$

Regarding to the above three image decomposition models, there are the following assumptions:

① u represents the true intensity function, which characterizes a physical property of the tissue being imaged and has the same value on the same type tissue.

② b represents the bias field function, which is a spatially smooth function and usually follows certain paths.

③ n is assumed to follow the Gaussian distribution in the three image models.

Various methods have been developed for intensity nonuniformity correction. One main group of methods realizes bias field estimation in a segmentation process. Pham and Prince [9] proposed an adaptive fuzzy c-means method by replacing the constant cluster centers with spatially varying functions to segment images in the presence of intensity nonuniformity. Ahmed *et al.* [10] presented a modified fuzzy c-means method by introducing a neighborhood term to influence the class membership of each pixel by its neighbors. Li *et al.* [11] derived a local intensity clustering property and used it to reformulate the Chan-Vese model for the segmentation of MRI images with intensity nonuniformity. Li *et al.* [12] proposed a segmentation model by representing the bias field by a linear combination of a given set of smooth basis functions to ensure its smoothly varying property. These methods usually rely on the assumptions of the image characteristics, most commonly, the number of tissues and location, and eliminate the small details and structures of the true intensity during tissue segmentation.

Another category of methods only estimates the bias field by directly working with the data. Sled *et al.* [13] proposed the nonparametric nonuniform normalization (N3) approach, which estimated the bias field by sharpening the image histogram using a Gaussian deconvolution and smoothing it with a B-spline strategy. The N3 algorithm was improved in [14] by a robust B-spline approximation routine and a modified hierarchical optimization scheme. Ashburner and Friston [15] used a linear combination of

low frequency discrete cosine transform basis functions to model the bias field, the coefficients of which are estimated by minimizing a weighted sum of squared differences between the data and the model. Vovk *et al.* [16] used a four-step iterative procedure to conduct a non-parametric inhomogeneity correction method, which was built on the characteristic space generated by the intensities and its second order derivatives. Manjón *et al.* [17] proposed an entropy-related cost function based on the combination of intensity and gradient image features for homogeneity measurement. Although these methods are able to estimate the bias field when images are corrupted by noise, the bias corrected data still contain noise, that means an additional denoising step is required before further quantitative analysis. Recently, Chang *et al.* [18] presented a high-order and L^0 regularized variational model based on model III (3) to simultaneously recover the true intensity and estimate the bias field. However, the method failed to remove the noise in the true intensity, the reason of which is twofold: the logarithmic transform changes the distribution of noise and the L^0 norm is sensitive to noise.

On the other side, the noise distribution of MRI data depends on the configuration of the acquisition system and the image reconstruction algorithm [19]. Considered the simplest system, single-coil systems, the noise of the magnitude MRI data follows a stationary Rician distribution. Although the Gaussian distribution can approximate Rician noise in high SNR regions, it is unable to model the noise distribution in low SNR regions [20]. There is around 60% underestimation of the true noise if we assume the the noise in MRI data follows a Gaussian distribution [1]. It is clear that modeling the noises in MRI data following a Rician distribution is more reasonable.

Since the pioneer work of Henkelman [21], numerous methods have been developed for MRI denoising. Gerig *et al.* [22] applied the nonlinear anisotropic filtering for MRI denoising, which may wipe the small features during denoising. Fernández *et al.* [23] proposed a denoising method by using the linear minimum mean square error estimator for images that follows a Rician noise. Krissian and Aja-Fernández [24] combined local linear minimum mean square error filters and partial differential equations for MRI denoising, which was extended to nonlocal version [25]. Wavelet transform-based approaches have also been developed for Rician denoising. Nowak [26] presented wavelet-domain filtering methods for Rician noise removal, which are

able to adapt to variations in both the signal and the noise. Getreuer *et al.* [27] used total variation regularization with a fidelity term involving the Rician probability. Liu *et al.* [28] developed a generalized total variation based denoising method, and used a local variance estimator method to calculate the spatially adaptive regularization parameters. Chen and Zeng [29] designed a strictly convex variational model for Rician denoising by adding an additional data fidelity term into the non-convex model [27]. Kang *et al.* [30] incorporated the convex fidelity term and a nonconvex high-order regularization term for denoising piecewise smooth images corrupted by Rician noises. Martin *et al.* [31] studied the properties of the TV-based Rician denoising model, and solved the nonsmooth noncovex minimization problem as the difference of convex functions. Although the aforementioned methods can deal with the Rician noise, they all ignore the intensity nonuniformity that may exist in the MRI data.

1.1. Goals of the Proposed Methodology

Based on the above discussion, our aim is to pursue a methodology that provides the same advantages of aforementioned methods but also overcomes their limitations. To be specific, the proposed method should not only be able to remove the noise, but also correct the intensity nonuniformity. Moreover, the noise need be modeled as a signal-dependent Rician noise rather than the additive Gaussian noise in model I (1), II (2) and III (3). Besides, it should be built up in the originally spatial domain as model I (1) or II (2), as the logarithmic transformation changes the distribution of noise.

1.2. Contributions and Organization

We propose a novel restoration model for MRI data, which are corrupted by both Rician noise and intensity nonuniformity. Following a MAP estimator, we derive an energy minimization problem under some mild assumptions. The proposal directly works on the multiplicative intrinsic relation of the true intensity and bias field to ensure the noise distribution is consistent with the real MRI data. For fast computation, we develop an alternating minimization algorithm by taking advantage of the separable structure of the proposed energy minimization problem. The solutions of all sub-minimization problems can be obtained by either the primal-dual splitting method or the closed-form

solution. We compared the proposed method with the state-of-the-art Rician denoising methods on the bias corrected MRI data showing a remarkably better behavior.

The paper is organized as follows. In Section 2, we introduce the notations and review the primal-dual algorithm for general convex optimization problem. In Section 3, we describe the proposed model, prove the existence of minimizers for the proposed model, and discuss its numerical algorithm. Numerical experiments details of the proposal were provided in Section 4 and Section 5. Finally, we concluded the paper by summarizing our contributions and discussing possible future works in Section 6.

2. Settings and Primal-Dual Algorithm

2.1. Discretization

Without loss of generality, we present a grayscale image as a two dimension matrix of size $N \times N$, the size of matrix here can also be $M \times N$. We denote X the Euclidean space $\mathbb{R}^{N\times N}$, which is equipped with the usual inner product and Euclidean norm as $\langle \cdot, \cdot \rangle$ and $\| \cdot \|_2$, respectively. The discrete gradient operator is a mapping $\nabla : X \to Y$, where $Y = X \times X$. For $u \in X$, ∇u is given by

$$(\nabla u)_{j,k} = \big((\mathring{D}_x^+ u)_{j,k}, (\mathring{D}_y^+ u)_{j,k}\big),$$

with

$$(\mathring{D}_x^+ u)_{j,k} = \begin{cases} u_{j,k+1} - u_{j,k}, & 1 \le k \le N-1, \\ u_{j,1} - u_{j,N}, & k = N, \end{cases}$$

$$(\mathring{D}_y^+ u)_{j,k} = \begin{cases} u_{j+1,k} - u_{j,k}, & 1 \le j \le N-1, \\ u_{1,k} - u_{N,k}, & j = N, \end{cases}$$

where $j, k = 1, \ldots, N$. Here we use $\mathring{D}_x^+$ and $\mathring{D}_y^+$ to denote forward difference operators with the periodic boundary conditions.

We also equip the space Y with the inner product $\langle \boldsymbol{p}, \boldsymbol{q} \rangle = \langle p^1, q^1 \rangle + \langle p^2, q^2 \rangle$ and the norm $\|\boldsymbol{p}\|_1 = \sum_{1\le j,k\le N} \sqrt{(p_{j,k}^1)^2 + (p_{j,k}^2)^2}$, and $\|\boldsymbol{p}\|_2 = \sqrt{\langle \boldsymbol{p}, \boldsymbol{p} \rangle}$. The discrete divergence operator $\mathrm{div} = -\nabla^*$ is a mapping $Y \to X$, where ∇^* is the adjoint of ∇. Given $\boldsymbol{p} \in Y$, we have

$$(\mathrm{div}\boldsymbol{p})_{j,k} = (\mathring{D}_x^- p^1)_{j,k} + (\mathring{D}_y^- p^2)_{j,k}$$

with

$$(\mathring{D}_x^- p^1)_{j,k} = \begin{cases} p^1_{j,k} - p^1_{j,k-1}, & 2 \le k \le N, \\ p^1_{j,1} - p^1_{j,N}, & k = 1, \end{cases}$$

$$(\mathring{D}_y^- p^2)_{j,k} = \begin{cases} p^2_{j,k} - p^2_{j-1,k}, & 2 \le j \le N, \\ p^2_{1,k} - p^2_{N,k}, & j = 1, \end{cases}$$

where $\mathring{D}_x^-$ and $\mathring{D}_y^-$ to denote backward difference operators with the periodic boundary conditions

2.2. The Primal-Dual Algorithm

In [32], Chambolle and Pock proposed a first-order primal dual algorithm for the following general optimization problem

$$\min_{v \in X} \; F(Kv) + G(v), \tag{4}$$

the primal-dual formulation of which is

$$\min_{v \in X} \max_{\boldsymbol{p} \in Y} \; \langle Kv, \boldsymbol{p} \rangle + G(v) - F^*(\boldsymbol{p}), \tag{5}$$

where $K : X \to Y$ is a continuous linear operator, $G : X \to [0, +\infty]$, $F : Y \to [0, \infty]$ are proper, convex, lower-semicontinuous functions, and F^* being itself the convex conjugate of F.

Both primal and dual variable are solved by the resolvent operator, which is defined for F as

$$x = (I + \tau \partial F)^{-1}(y) = \arg\min_x \left\{ F(x) + \frac{1}{2\tau} \|x - y\|_2^2 \right\}.$$

The primal-dual algorithm for (5) is summarized in Algorithm 1.

We take the ROF model [33] for image denoising as an example, and derive its primal-dual scheme. The primal-dual formulation of ROF model is defined as follows

$$\min_{v} \max_{\|\boldsymbol{p}\|_\infty \le 1} \; -\alpha \langle v, \mathrm{div} \boldsymbol{p} \rangle + \frac{1}{2} \|f - v\|_2^2,$$

where $\|\boldsymbol{p}\|_\infty$ denotes the L^∞ vector norm. For the primal variable, the resolvent operator is equivalent to solve the following minimization problem, which is trivially given

Algorithm 1 The Primal-Dual Algorithm

1. Initialization: Choose $\tau, \nu > 0$, $\theta \in [0,1]$, $v^0 \in X$, $\boldsymbol{p}^0 \in Y$ and $\bar{v}^0 = v^0$;
2. Iterations ($k \geq 0$): Update v^{k+1}, $\boldsymbol{p}^{k+1}$, $\bar{v}^{k+1}$

$$\begin{cases} \boldsymbol{p}^{k+1} = (I + \nu\partial F^*)^{-1}(\boldsymbol{p}^k + \nu K\bar{v}^k), \\ v^{k+1} = (I + \tau\partial G)^{-1}(v^k - \tau K^*\boldsymbol{p}^{k+1}), \\ \bar{v}^{k+1} = v^{k+1} + \theta(v^{k+1} - v^k). \end{cases}$$

as

$$\begin{aligned} v &= \arg\min_v \Big\{ -\alpha\langle v, \mathrm{div}\boldsymbol{p}\rangle + \frac{1}{2}\|f - v\|_2^2 + \frac{1}{2\tau}\|v - v^k\|_2^2 \Big\} \\ &= \frac{\tilde{v} + \tau f}{1 + \tau}, \end{aligned} \tag{6}$$

where $\tilde{v} = v^k + \tau\alpha\mathrm{div}\boldsymbol{p}^{k+1}$.

For the dual variable, the resolvent operator is equivalent to solve the following maximization problem

$$\begin{aligned} \boldsymbol{p} &= \arg\max_{\|\boldsymbol{p}\|_\infty \leq 1} \alpha\langle\nabla\bar{v}, \boldsymbol{p}\rangle - \frac{1}{2\nu}\|\boldsymbol{p} - \boldsymbol{p}^k\|_2^2 \\ &= \mathcal{P}(\tilde{\boldsymbol{p}}), \end{aligned} \tag{7}$$

where $\tilde{\boldsymbol{p}} = \boldsymbol{p}^k + \nu\alpha\nabla\bar{v}$, and $\mathcal{P}$ is projector onto the L^2-normed unit ball, i.e.,

$$\mathcal{P}(\tilde{\boldsymbol{p}}) = \frac{\tilde{\boldsymbol{p}}}{\max(1, |\tilde{\boldsymbol{p}}|)}.$$

Remark 2.1. *The primal-dual algorithm 1 is convergent if $\tau\nu\alpha^2 < \frac{1}{8}$ [34]. In our numerical experiments, we tune α empirically, and fix $\tau = 0.015/\alpha$ and $\nu = 8/\alpha$. Besides, we also fix $\theta = 1$ for all implementations.*

3. Rician Noise and Intensity Nonuniformity Correction (NNC) Model

3.1. The Proposed MAP-based model

Assume the observed MRI data are corrupted by a Rician distributed noise as

$$p(f|v,\sigma) = \frac{f}{\sigma^2} e^{-\frac{v^2+f^2}{2\sigma^2}} I_0\Big(\frac{vf}{\sigma^2}\Big), \tag{8}$$

where f denotes the value in obtained magnitude signal, v represents the noise-free signal, σ is the standard deviation of Gaussian noise in complex domain, and I_0 is the modified Bessel function of the first kind with order zero. We aim to maximize $P(v|f)$, which gives us the following maximum a posterior (MAP) estimator

$$\hat{v} = \arg\max_v P(v|f) = \arg\max_v \frac{P(f|v)P(v)}{P(f)}$$

Since $P(f)$ is a constant and maximizing $P(v|f)$ amounts to minimizing the log-likelihood, we have

$$\hat{v} = \arg\min_v -\log\big(P(f|v)\big) - \log\big(P(v)\big)$$

According to (8), the additive noise in each pixel following a Rician distribution, we have

$$-\log\big(P(f|v)\big) = \int_\Omega \frac{1}{2\sigma^2}v^2(x) - \log I_0\Big(\frac{f(x)v(x)}{\sigma^2}\Big)dx, \tag{9}$$

and we assume v follows a TV prior [35], i.e.,

$$P(v) \propto \exp(-\alpha \int_\Omega |\nabla v|dx). \tag{10}$$

Meanwhile, we assume that the noise-free image v is a multiplicative intrinsic combination of a true intensity function u and a bias field function b, i.e., $v = ub$. There is

$$P(v) = P(v|ub)P(ub).$$

Suppose the difference between v and ub follows a Gaussian distribution, that is

$$P(v|ub) \propto \exp\big(-\frac{\lambda}{2}\int_\Omega (v-ub)^2dx\big), \tag{11}$$

where λ is a positive scalar. Furthermore, we assume that u and b are independent and identically distributed (i.i.d). Since u represents the true intensity, which can be approximated by a piecewise constant function, it follows a TV prior. Due to the spatial smoothness of the bias field function b, there should not present discontinuities across lines in the solution of b. Thus, we assume the derivative of b is square integrable [36]. Therefore, we have

$$P(u) \propto \exp\big(-\beta\int|\nabla u|dx\big), \quad \text{and} \quad P(b) \propto \exp\big(-\frac{\gamma}{2}\int|\nabla b|^2dx\big), \tag{12}$$

where β, γ are positive constants. Together with (9), (10), (11) and (12), we are able to obtain the following restoration model for MRI data

$$\begin{aligned}\inf_{v,u,b} \quad & \int_\Omega \left(\frac{1}{2\sigma^2}v^2 - \log I_0\big(\frac{fv}{\sigma^2}\big)\right)dx + \alpha\int_\Omega |\nabla v|dx \\ & + \frac{\lambda}{2}\int_\Omega (v-ub)^2dx + \beta\int_\Omega |\nabla u|dx + \frac{\gamma}{2}\int_\Omega |\nabla b|^2dx.\end{aligned} \tag{13}$$

By denoting

$$D(v) := \frac{1}{2\sigma^2}\|v\|_2^2 - \Big\langle \log I_0\big(\frac{fv}{\sigma^2}\big), 1\Big\rangle,$$

the proposed model (13) can be rewritten as the following discrete formula

$$\min_{\substack{0\le v\le 255\\ 0\le u\le 255, b}} E(v,u,b) := D(v) + \frac{\lambda}{2}\|v-ub\|_2^2 + \alpha\|\nabla v\|_1 + \beta\|\nabla u\|_1 + \frac{\gamma}{2}\|\nabla b\|_2^2 + \frac{\tau}{2}\|b\|_2^2, \tag{14}$$

where the box constraints on v and u are widely used in image processing [29], and the last term is introduced with a positive parameter τ for the theoretical setting.

Although the energy functional (14) is non-convex, it is still available to show the existence of minimizers. Inspired by the work in [31] on Rician noisy data term, we have

Lemma 3.1. *Let Ω be an open, bounded domain in $\mathbb{R}^N (N \ge 2)$ with Lipschitz boundary. Assume $f(x) \ge 0, a.e.\ x \in \Omega$ and fixed parameters $\lambda, \alpha, \beta, \gamma, \tau > 0$ and $\sigma^2 \ne 0$, then the functional $E(v,u,b)$ defined in (14) is coercive.*

Proof. According to Lemma 2 in [31], $D(v)$ is coercive in $L^2(\Omega)$. We can verify that $E(v,u,b) \to \infty$ as $\|(v,u,b)\|_2 \to \infty$ [1]. Thus, the functional $E(v,u,b)$ is coercive in $BV(\Omega) \times BV(\Omega) \times H^1(\Omega)$. □

The proof of coerciveness can be used to show that the energy minimization problem (14) has, at least, one positive, nontrivial solution, that is

Theorem 3.1. *Suppose $f \in L^2(\Omega)$ is nonnegative and $\lambda, \alpha, \beta, \gamma, \tau > 0$, then the problem (14) has at least one solution $(v^*, u^*, b^*) \in BV(\Omega) \times BV(\Omega) \times H^1(\Omega)$.*

Proof. See Appendix. □

[1] $\|(\cdot,\cdot,\cdot)\|_2$ is the usual ℓ^2 norm defined as $\|(v,u,b)\|_2 = \sqrt{v^2+u^2+b^2}$.

3.2. Primal-Dual based Alternating Minimization Algorithm

Since the variables v, u and b are coupled together, an accurate joint minimization can be costly. Thus, we adopt the alternating direction minimization to utilize the separability structure of (14), through which one can obtain the minimizer approximately [37, 38]. We propose an alternating minimization algorithm to solve (14). Starting from initial guesses of u^0 and b^0, the algorithm computes a sequence of iterates as

$$v^1, u^1, b^1, v^2, u^2, b^2, \ldots, v^k, u^k, b^k, \ldots$$

see Algorithm 2.

Algorithm 2 Alternating Minimization of the NNC Model

1. Initialization: v^0, u^0, b^0;
2. For $k = 0, 1, \ldots$: compute v^{k+1}, u^{k+1} and b^{k+1} from

$$\begin{cases} v^{k+1} = \arg\min\limits_{0\le v\le 255} \; D(v) + \dfrac{\lambda}{2}\|v - u^k b^k\|_2^2 + \alpha\|\nabla v\|_1; & (15) \\ u^{k+1} = \arg\min\limits_{0\le u\le 255} \; \dfrac{\lambda}{2}\|v^{k+1} - u b^k\|_2^2 + \beta\|\nabla u\|_1; & (16) \\ b^{k+1} = \arg\min\limits_{b} \; \dfrac{\lambda}{2}\|v^{k+1} - u^{k+1} b\|_2^2 + \dfrac{\gamma}{2}\|\nabla b\|_2^2 + \dfrac{\tau}{2}\|b\|_2^2; & (17) \end{cases}$$

3. Measure the relative residuals and stop iteration if they are small than the tolerance

$$\max\left(\frac{\|u^{k+1} - u^k\|_2^2}{\|u^{k+1}\|_2^2}, \frac{\|b^{k+1} - b^k\|_2^2}{\|b^{k+1}\|_2^2}\right) \le tol.$$

Remark 3.1. *A multi-resolution scheme was implemented to accelerate the algorithm, which estimated the the variables on coarse resolution layers and used the corresponding interpolation values as initialization for the next layer [39]. Three resolution layers were used for all experiments. We set* $tol = 5e-4$ *on coarse layers,* $tol = 5e-5$ *on the fine layer for synthetic MRI data, and* $tol = 5e-3$ *on coarse layers,* $tol = 1e-4$ *on the fine layer for real MRI data.*

Now we are left the minimization problems (15), (16) and (17) to address. The subminimization problem (15) and (16) are of the same kind and could be solved efficiently by many optimization methods, such as the split Bregman method, the augmented

Lagrangian method and the primal-dual method. We adopt the primal-dual Algorithm 1, which yields a simple iteration scheme for our problem.

3.2.1. Sub-minimization with respect to v

The primal-dual formulation of (15) is given as

$$\min_{0\leq v\leq 255}\max_{\|\boldsymbol{p}\|_\infty\leq 1} D(v)+\frac{\lambda}{2}\|v-u^kb^k\|_2^2-\alpha\langle v,\mathrm{div}\boldsymbol{p}^k\rangle.$$

For the primal variable v, it gives a nonlinear minimization problem

$$\min_{0\leq v\leq 255} D(v)+\frac{\lambda}{2}\|v-u^kb^k\|_2^2-\alpha\langle v,\mathrm{div}\boldsymbol{p}^k\rangle+\frac{1}{2\tau_v}\|v-v^{k-1}\|_2^2,$$

which can be solved by Newton's method [38, 27]. Denote

$$g(v)=\frac{1}{\sigma^2}v-\frac{I_1\left(\frac{vf}{\sigma^2}\right)}{I_0\left(\frac{vf}{\sigma^2}\right)}\frac{f}{\sigma^2}+\lambda(v-u^kb^k)-\alpha\mathrm{div}\boldsymbol{p}^k+\frac{1}{\tau_v}(v-v^{k-1}),$$

where I_1 is the first-order modified Bessel function of the first kind. As only one iteration of Newton's method is used, the solution to v can be expressed as follows

$$v^{k+1}=v^k-\frac{g(v^k)}{g'(v^k)}. \tag{18}$$

For the dual variable $\boldsymbol{p}$, it is exactly the same minimization as the dual problem of ROF model, the solution of which is given as

$$\boldsymbol{p}^{k+1}=\mathcal{P}(\boldsymbol{p}^k+\nu_p\alpha\nabla v^{k+1}).$$

Here, τ_v and ν_p are two positive constants, which are set as $\tau_v=0.015/\alpha$ and $\nu_p=8/\alpha$.

Remark 3.2. *For efficiency, we approximate I_1/I_0 by a cubic rational polynomial as [27] in the numerical implementation, i.e.,*

$$\frac{I_1(t)}{I_0(t)}\approx\frac{t^3+0.950037t^2+2.38944t}{t^3+1.48937t^2+2.57541t+4.65314}.$$

3.2.2. Sub-minimization with respect to u

The sub-minimization problem of u can also be solved by the primal-dual algorithm, which is rewritten as

$$\min_{0\leq u\leq 255}\max_{\|\boldsymbol{q}\|_\infty\leq 1}\ \frac{\lambda}{2}\|v^{k+1}-ub^k\|_2^2-\beta\langle u,\mathrm{div}\boldsymbol{q}^k\rangle.$$

For the primal variable u, we can directly obtain its minimizer as follows

$$u^{k+1}=\frac{u^k+\tau_u\lambda b^k v^{k+1}+\tau_u\beta\mathrm{div}\boldsymbol{q}^k}{1+\tau_u\lambda(b^k)^2}, \tag{19}$$

Similarly, the solution to the dual variable $\boldsymbol{q}$ can be achieved according to (7), i.e.,

$$\boldsymbol{q}^{k+1}=\mathcal{P}(\boldsymbol{q}^k+\nu_q\beta\nabla u^{k+1}).$$

Similarly, τ_u and ν_q are two positive constants, which are chosen as $\tau_u=0.015/\beta$ and $\nu_q=8/\beta$.

3.2.3. Sub-minimization with respect to b

We apply a fixed-point approach to the mix term of ub to linearize the coefficient of b and reformulate the sub-minimization problem as follows

$$\min_b\ \lambda\langle u^{k+1}b,u^{k+1}b^k-v^{k+1}\rangle+\frac{\gamma}{2}\|\nabla b\|_2^2+\frac{\tau}{2}\|b\|_2^2+\frac{1}{2\eta}\|b-b^k\|_2^2.$$

The Euler-Lagrange equation associated with (3.2.3) gives us a linear equation

$$\big((1+\eta\tau)\mathcal{I}-\eta\gamma\Delta\big)b=\eta\lambda u^{k+1}(v^{k+1}-u^{k+1}b^k)+b^k,$$

where $\mathcal{I}$ is the identity operator. Relying on the periodic boundary condition, it allows us to use the fast Fourier transform (FFT) to solve the above equation. Denoting $\mathcal{F}(b)$ as the Fourier transform of b, we have the solution to b as follows

$$b^{k+1}=\mathcal{F}^{-1}\left(\frac{\eta\lambda\mathcal{F}(u^{k+1})\mathcal{F}(v^{k+1})-\eta\lambda\mathcal{F}\big((u^{k+1})^2b^k\big)+\mathcal{F}(b^k)}{(1+\eta\tau)\mathcal{I}-\eta\gamma\mathcal{F}(\Delta)}\right), \tag{20}$$

where $\mathcal{F}(\Delta)=\mathring{D}_x^-\mathring{D}_x^+ + \mathring{D}_y^-\mathring{D}_y^+$ and η is a positive constant fixed as $\eta=0.1$.

4. Material and Methods

In this section, we introduce the MRI data sets, and the implementation details of our method and the comparison methods used in the validation.

4.1. Materials

The following data sets are used for comparison:

- *Synthetic MRI data:* Three MRI slices from Brainweb simulated database [40] with different modalities, i.e., PD-, T_1- and T_2-weighted MRI data, are used for evaluation. More specifically, the noise level=[5%, 7%, 9%] for three types MRI data. On the other side, all MRI data are also contaminated by intensity nonuniformity (INU), i.e., the PD-weighted MRI data is with INU of 40%; the T_1-weighted MRI data is with INU of 100% and the T_2-weighted MRI data is with two additional bias field profiles, which are denoted as INU 1 and INU 2.

- *Realistic MRI data:* We select one slice of 7T T_1-weighted scan acquired by Turbo Field Echo (TFE) sequence, which is downloaded from http://multimodal.projects.nitrc.org/MMRR- 3T7T-2-1 multimodal.tar.gz. Another two 2D MRI images "Lumbar spine" and "Liver" are also tested.

4.2. Methods

We discuss the performance of proposal in Rician noise removal by comparing it with 4 other methods, the implementation details of which are provided as follows

- MSE: *linear minimum mean square error estimator* [23]. The local neighborhood of 5×5 voxels was used for PD-, T_1- and T_2-weighted MRI data.

- TVM: *total variation based variational model* [27]. We tuned the data fidelity term parameter λ in $\lambda \in [4, 14]$ according to the noise level and the strength of bias field.

- LGTV: *locally generalized total variation* [28]. We fixed the parameter $\varepsilon = 1$, the maximum iteration as 1000, and the step size as 0.05. The exponents parameter γ was chosen as $\gamma = 0.8$ for the PD- and T_1-weighted MRI data, $\gamma = 0.85$ for the T_2-weighted MRI data of INU 1 and $\gamma = 0.75$ for the T_2-weighted MRI data of INU 2, respectively.

- CTV: *convex total variation based model* [29]. We set $\beta = 8/\gamma, \tau = 0.015/\gamma$ and tuned the regularization parameter γ in $\gamma \in [0.08, 0.4]$ depending on the noise level.

- NNC: There are several parameters in our model, some of which can be fixed, i.e., $\lambda = 0.04$, $\tau = 1e-5$ for all experiments and $\gamma = 14$, $\gamma = 4$, $\gamma = 7.5$, $\gamma = 10$ for PD-, T_1-, T_2-weighted and real MRI data, respectively. The left parameters α and β are closely related to the severity of noise and intensity nonuniformity, which will be specified in the experiments.

For a fair comparison, we use N4 algorithm [14] to remove the bias field before applying the denoising methods for T_1- and T_2-weighted MRI data, which is performed using Advanced Normalization Tools (ANTs). The parameters are kernel fwhm= 0.15; Wiener filter noise= 0.1; number of iterations= 50; and fitting levels= 4.

For quantitative analysis, we use the *Peak Signal-to-Noise Ratio* (PSNR) and Mean *Structural Similarity index* (MSSIM) [41] for evaluating the denoising results. The *Coefficient of Variations* (CV) is used to quantify the degree of intensity nonuniformity, which is defined on tissue T as

$$\text{CV(T)} = \frac{\sigma(\text{T})}{\mu(\text{T})},$$

where σ and μ denote the standard deviation and the mean of the intensities.

4.3. Noise Estimation

Automatic methods have been developed for stationary and non-stationary Rician noise estimation. We refer the interested readers to see Ref. [42] and the references therein for more information. Figure 1 depicts the standard variation σ obtained by the the object-based method [43] for a T_1-weighted MR image corrupted by different levels of Rician noise and INU. It reveals that σ increases as noise increases and decreases as INU increases. Figure 2 provides the estimated noise maps using the non-stationary noise estimation method [44] for the same images, where the trend of the change on σ follows the same pattern as the case of stationary noise estimation. **It straightforward to conclude that the existence of intensity nonuniformity may lead to the underestimation of the noise.** Due to the existence of intensity nonuniformity influences

the estimation of noise, we simply use the stationary noise estimation model in the numerical experiments unless noted otherwise.

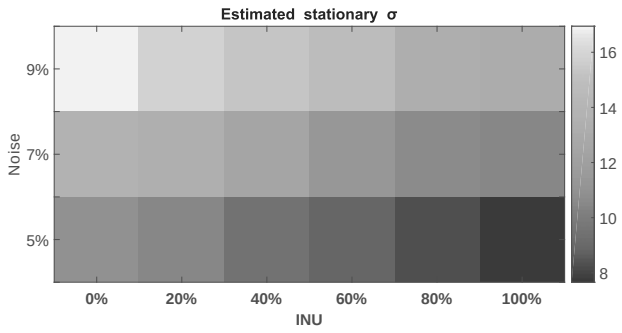

Figure 1: The estimated stationary noise σ for a T_1-weighted image with different noise levels and INU.

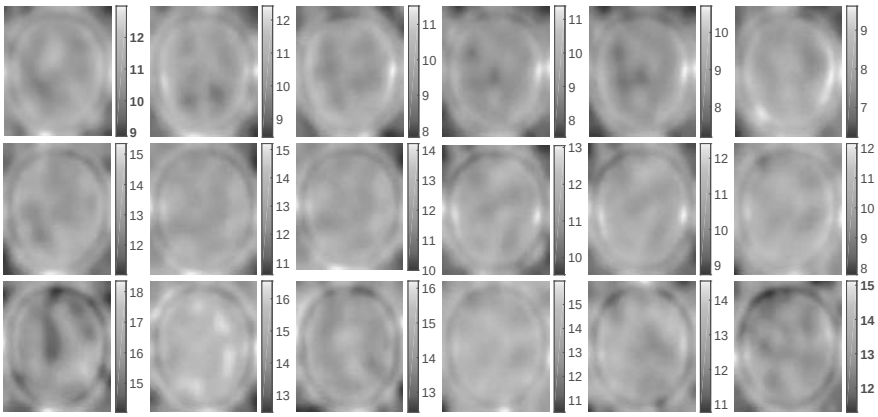

(a) 0% INU (b) 20% INU (c) 40% INU (d) 60% INU (e) 80% INU (f) 100% INU

Figure 2: The estimated non-stationary noise σ for a T_1-weighted image with different noise levels and INU. Row one to three are of noise 5%, 7%, and 9%, respectively.

5. Experiments and Results

5.1. Synthetic MRI Experiments

As the first experiment, we compare the NNC with the aforementioned MRI denoising methods on PD-weighted MRI data. The comparison results of 5% Rician are

displayed in Figure 3. Although the intensity nonuniformity is not apparent visually, we can figure out its existence in the 1D profiles. It is obviously shown that the intensity values obtained by the NNC model is more structurally similar to the ground truth, especially in the pink inset. The denoising accuracy is quantitatively verified by evaluating results in terms of PSNR, MSSIM and the CV of white matter obtained, as shown in Table 1. Both visual results and the CV values of white matter demonstrate that all compared algorithms fail to remove the bias field, while the NNC model is able to remove the noise and intensity nonuniformity simultaneously.

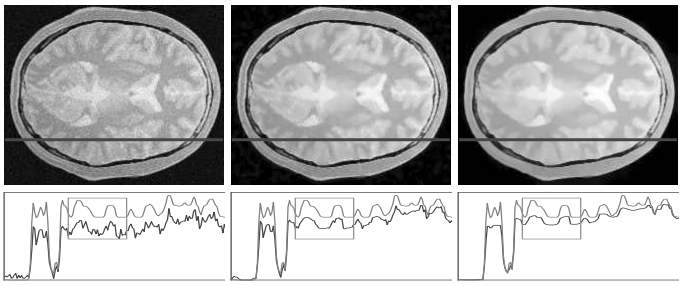

(a) Original image (b) MSE (c) TVM

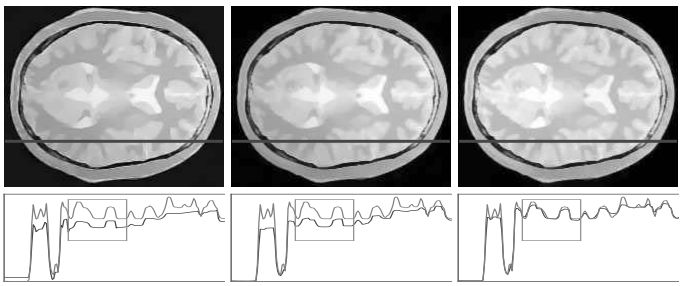

(d) LGTV (e) CTV (f) NNC

Figure 3: The recovered results and their associated 1D profiles of PD-weighted MRI data with noise 5% and INU 40%, where the red line denotes the ground truth. The parameter for TVM model is $\lambda = 8$; CTV model is $\gamma = 0.15$ and our NNC model is $\alpha = 0.12$, β =0.003.

Secondly, we carry out the experiments on T_1-weighted images, where more intensive intensity nonuniformity are employed. For a fair comparison, we implement N4 algorithm to correct the intensity nonuniformity, the results of which are used as the

Table 1: PSNR, MSSIM and CV of white matter of PD-weighted MRI data with different Rician noises and 40% INU.

Methods	5%			7%			9%		
	PSNR	MSSIM	CV	PSNR	MSSIM	CV	PSNR	MSSIM	CV
Original	16.3238	0.8154	8.7391	14.7227	0.7412	10.5060	13.6349	0.6719	12.4232
MSE	21.1140	0.9033	6.7615	19.3569	0.8736	6.9257	16.8242	0.8328	7.2321
TVM	22.8612	0.9054	6.2598	22.4652	0.8849	6.2521	21.9853	0.8588	6.4309
LGTV	21.2072	0.8707	6.5656	20.3295	0.8514	6.4307	18.2572	0.8224	6.8260
CTV	22.4421	0.8994	6.4885	21.8129	0.8871	6.6294	21.1968	0.8654	6.9145
NNC	**26.1919**	**0.9170**	**4.0239**	**25.2063**	**0.9003**	**4.1097**	**24.5553**	**0.8797**	**4.3789**

input for all algorithms except NNC. The PSNR, MSSIM and CV are listed in Table 2, which indicate that N4 algorithm is able to remove the bias field to a certain extent. However, when the noise increases, the improvement of N4 algorithm becomes limited. On the other hand, we conduct a comparative experiment using σ obtained by both the stationary and non-stationary noise estimation method. Table 2 reveals that there is no significant difference in PSNR, MSSIM and CV for all algorithms no matter what noise estimation method is used. Thus, we can just use the stationary noise estimation method when images are corrupted by both noise and intensity nonuniformity.

Figure 4 depicts the visual results and the surface plots of 7% Rician noise obtained using the stationary noise estimation. We see that, the MSE, TVM, LGTV and CTV model produce similar visual results, which still exhibit the intensity nonuniformity in the middle region (marked by the red box). On the other side, the NNC model is capable to provide denoising result with homogenous intensity, which gives the most similar surface plot as obtained from the ground truth (Figure 4 (c)). Although the results of comparative algorithms are obtained based on bias corrected data, the best PSNR and MSSIM are still achieved by our NNC model. Since the NNC, TVM and CTV model share the same regularization term, the comparison results are readily to demonstrate the advantages of modeling noise and bias field simultaneously.

Thirdly, we conduct another experiment on T_2-weighted MRI data, in which we further amplify the bias fields. Similarly, we use N4 algorithm to correct the intensity nonuniformity before implement the compared denoising algorithms. As shown in Table 3, N4 algorithm totally lose its effect when the bias field is increased from

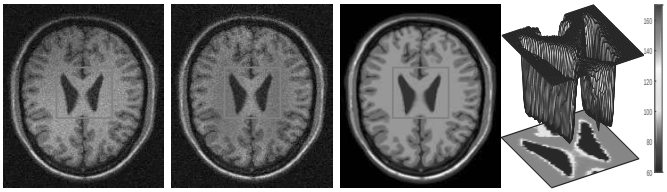

(a) Original image (b) N4 corrected (c) Ground truth and magnified view

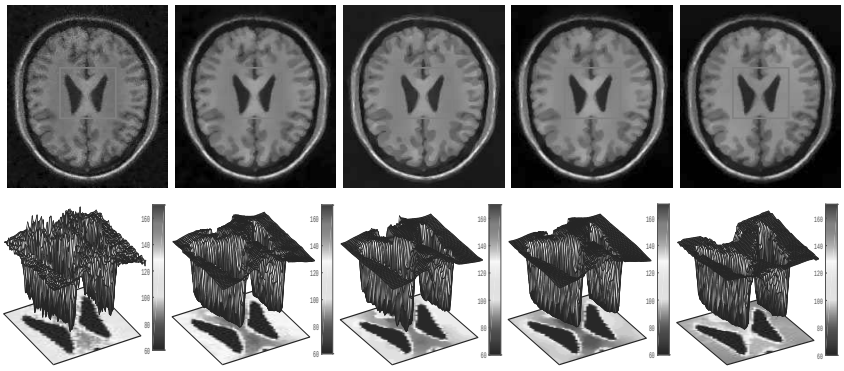

(d) MSE (e) TVM (f) LGTV (g) CTV (h) NNC

Figure 4: The recovered images and their associated surface plots of T_1-weighted MRI data with noise 7% and INU 100%. The parameter for the TVM is $\lambda = 8$, the CTV model is $\gamma = 0.18$, the NNC model is $\alpha = 0.11$, $\beta = 0.002$.

INU 1 to INU 2. Meanwhile, the PSNR, MSSIM and CV significantly drop for all compared algorithms, while the values obtained by the NNC model only slightly decreases. Figure 5 and 6 presents the original images, N4 corrected images, the true and the estimated bias field, and the restoration results. Apparently, the estimated basis field is very close to the ground truth of INU, which indicates that our proposal can correctly estimate distribution of the INU. Both restored results and the difference images between the restored images illustrate that significant bias fields are left in the difference images of the compared methods. As observed, when the bias field becomes intense, the performance of the N4 algorithm is far from being satisfied. Happily, our NNC model is shown to be robust with noise and bias field by both quantitative and visual results. Thus, it is a good way to consider both noise and intensity nonuniformity

Table 2: PSNR, MSSIM and CV of white matter of T_1-weighted MRI data with estimated stationary and non-stationary Rician noises and 100% INU, where N4 denotes the image corrected by the N4 algorithm.

INU	Methods	5%			7%			9%		
		PSNR	MSSIM	CV	PSNR	MSSIM	CV	PSNR	MSSIM	CV
	Original	19.2471	0.7507	12.9733	18.2573	0.6966	14.8417	17.7518	0.6540	16.5297
	N4	22.8128	0.7935	9.6305	20.8579	0.7393	12.2887	19.5991	0.6893	14.4233
Stationary	MSE	23.6754	0.8224	7.6191	22.0643	0.7893	8.7053	21.1621	0.7628	9.1400
	TVM	25.3463	0.8542	6.5555	24.8452	0.8410	7.2671	24.7781	0.8288	7.3330
	LGTV	23.8220	0.8193	6.1189	23.2543	0.8086	6.6827	22.6086	0.7905	7.6223
	CTV	25.4766	0.8587	6.4084	25.2772	0.8423	6.9673	24.9513	0.8335	7.2977
	NNC	**26.7530**	**0.8854**	**5.9711**	**25.8609**	**0.8665**	**6.5305**	**25.4795**	**0.8571**	**6.9870**
Non-Stationary	MSE	23.7224	0.8238	7.4736	22.0438	0.7888	8.7328	21.1157	0.7613	9.2455
	TVM	25.6274	0.8541	6.3921	25.0627	0.8426	7.2384	24.8383	0.8304	7.3061
	LGTV	23.8199	0.8193	6.1202	23.2521	0.8086	6.6834	22.6219	0.7908	7.6357
	CTV	25.7635	0.8584	6.2324	25.3209	0.8451	6.9318	25.0045	0.8354	7.2534
	NNC	**26.6294**	**0.8824**	**6.0929**	**26.0230**	**0.8676**	**6.6224**	**25.4898**	**0.8566**	**7.1022**

simultaneously for MRI image restoration.

Table 3: PSNR, MSSIM and CV of white matter of T_2-weighted MRI data with different Rician noises and INU, where N4 denotes the image corrected by the N4 algorithm.

INU	Methods	5%			7%			9%		
		PSNR	MSSIM	CV	PSNR	MSSIM	CV	PSNR	MSSIM	CV
1	Original	20.7964	0.8702	20.7081	18.8857	0.8165	25.8893	17.6169	0.7661	30.5574
	N4	22.3763	0.8903	18.8371	19.1328	0.8267	24.7748	17.8761	0.7768	29.8008
	MSE	23.3333	0.9145	12.8938	20.0636	0.8667	15.0745	18.9240	0.8310	16.4763
	TVM	24.6692	0.9165	10.3348	22.0283	0.8715	10.8940	20.6052	0.8312	11.1495
	LGTV	22.9047	0.8865	10.1494	20.7786	0.8510	10.7599	19.5785	0.8232	11.2603
	CTV	24.2946	0.9264	11.4358	21.4414	0.8736	12.8785	19.9485	0.8420	14.2576
	NNC	**26.6807**	**0.9351**	**9.1038**	**24.9930**	**0.9150**	**10.0893**	**23.2241**	**0.8919**	**11.1251**
2	Original	18.6426	0.8295	26.8615	17.5107	0.7789	31.4133	16.6272	0.7317	35.4346
	N4	18.4949	0.8207	26.3754	17.3157	0.7698	31.0898	16.4062	0.7218	34.7547
	MSE	18.6563	0.8320	22.8199	17.6048	0.7910	25.0835	16.7504	0.7519	25.8876
	TVM	18.9192	0.8280	20.1225	18.1695	0.7931	20.6308	17.4990	0.7569	19.9863
	LGTV	18.2038	0.8120	20.8612	17.3678	0.7790	21.3264	16.7184	0.7481	21.6085
	CTV	18.6296	0.8256	21.3165	17.7538	0.7752	21.9710	17.1476	0.7544	22.1311
	NNC	**25.4554**	**0.9281**	**9.4243**	**24.0328**	**0.9043**	**10.2049**	**22.1206**	**0.8683**	**11.5281**

In the end, we present the outputs of the NNC method for PD-, T_1- and T_2-weighted MRI images of 7% Rician noise in Figure 7, which primely shows that the noise-

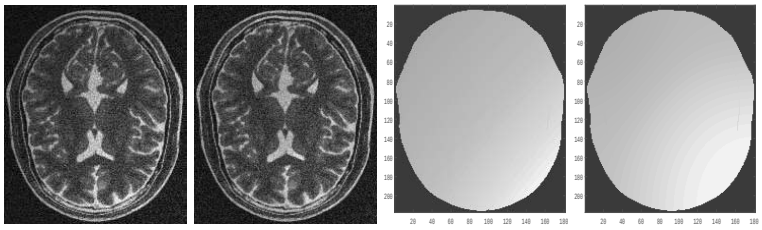

(a) Original image (b) N4 corrected (c) True INU1 (d) Estimated INU1

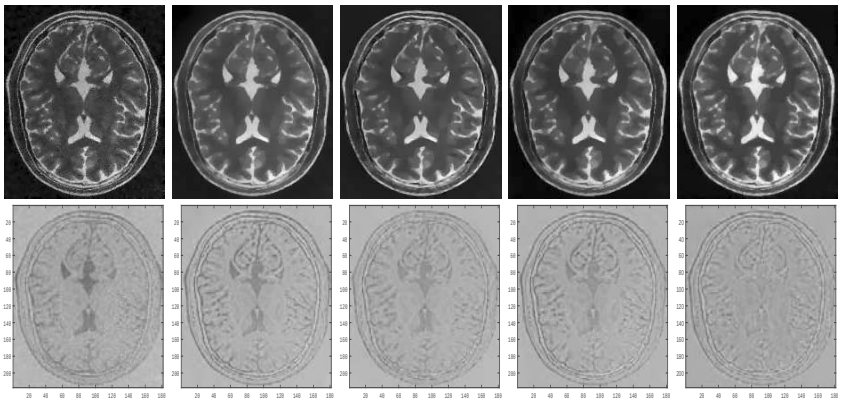

(f) MSE (g) TVM (h) LGTV (i) CTV (j) NNC

Figure 5: The recovered images and their associated difference images of T_2-weighted MRI data with noise 9% and INU 1. The parameter for the TVM is $\lambda = 10$, the CTV model is $\gamma = 0.12$, and the NNC model is $\alpha = 0.08$, $\beta = 0.0002$.

free image v has been well decomposed into the true intensity u and the smooth bias field b for all image modalities. The improvement of the image quality can also be demonstrated by comparing the histograms of the original images and the solution u, as shown in Figure 7 (e). There are separated peaks in the histograms of the solution u, corresponding to the background, cerebrospinal fluid, gray matter and white matter, while the histograms of the original images do not have such well-defined peaks due to the existence of the bias field. Besides, we use the T_1-weighted MRI image in Figure 7 as an example, and plot the relative errors in Figure 8. It is shown that both the relative error of v, u and b decay as the iteration increase, which demonstrate that our model converges well numerically.

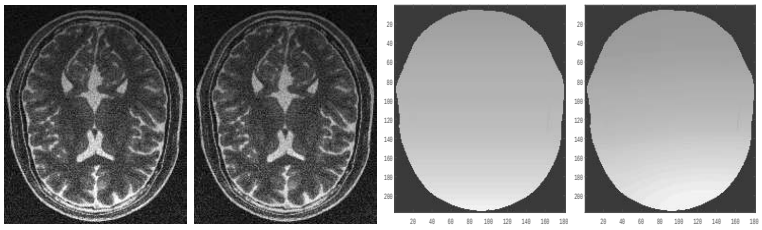

(a) Original image (b) N4 corrected (c) True INU2 (d) Estimated INU2

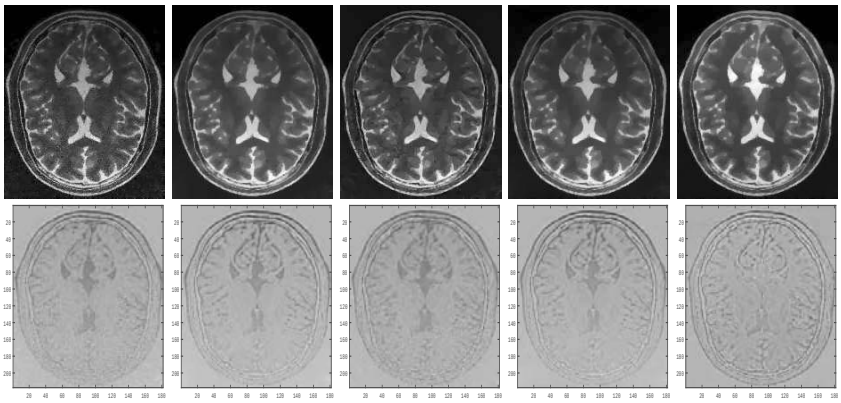

(f) MSE (g) TVM (h) LGTV (i) CTV (j) NNC

Figure 6: The recovered images and their associated difference images of T_2-weighted MRI data with noise 9% and INU 2. The parameter for the TVM is $\lambda = 10$, the CTV model is $\gamma = 0.12$, and the NNC model is $\alpha = 0.11$, $\beta = 0.002$.

5.2. Real MRI Experiments

The last subsection is devoted to test our method on realistic MRI data. For 7T SENSE MRI data, we add the Rician noise of 5%, where the estimated σ is $\sigma = 2$. Results are depicted in Figure 9, which demonstrate that all denoising methods can remove the noise quite well. In particular, the contour plot indicates that there exists both noise and bias field in the original image as the isolines can not completely identify the boundary of the white matter in the magnified region. It is obvious shown that our NNC method gives the most satisfactory denoising result, the isolines of which are complete, clear and smooth. Other methods, such as the MSE, TVM and CTV model, fail to identify the boundary of white matter from gray matter. The contour plot of

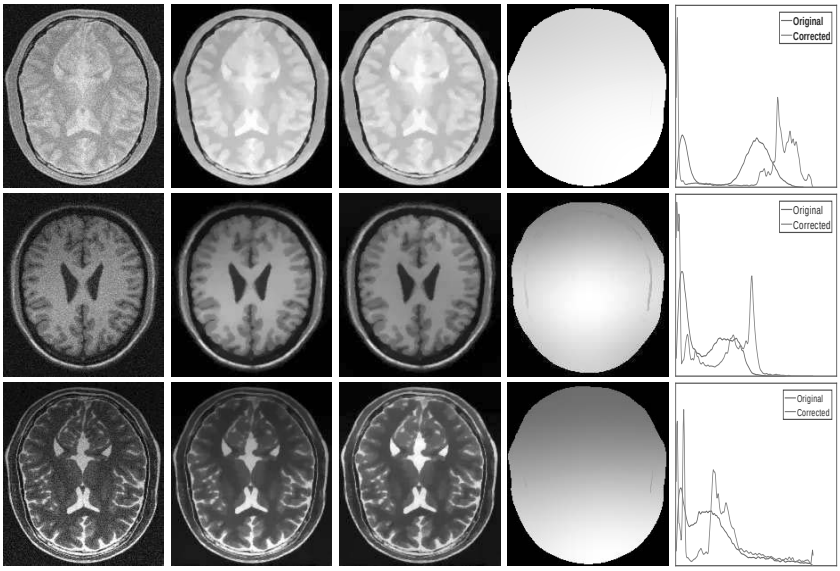

(a) f (b) v (c) u (d) b (e) Histograms

Figure 7: The recovered results and histograms of the NNC model for PD-, T_1-, and T_2-weighted MRI data with noise 7%.

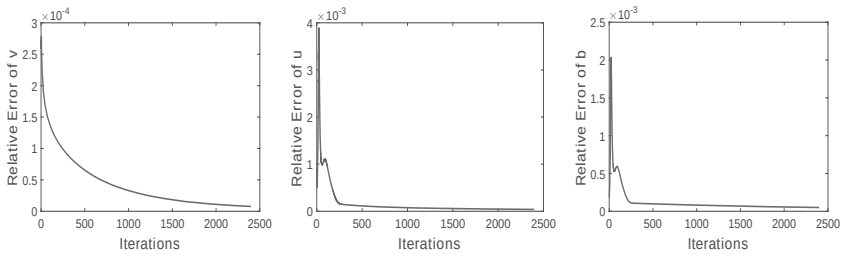

(a) v (b) u (c) b

Figure 8: The relative error of v, u and b of the NNC model for T_1-weighted MRI data in 7.

LGTV shows that the LGTV gives a over-smooth denoising result.

Another experiment is conducted on two MRI images of Liver and Lumbar spine, both of which exhibit obvious intensity nonuniformity. For the liver MRI experiment in Figure 10, we can find that the intensities within each tissue become more homo-

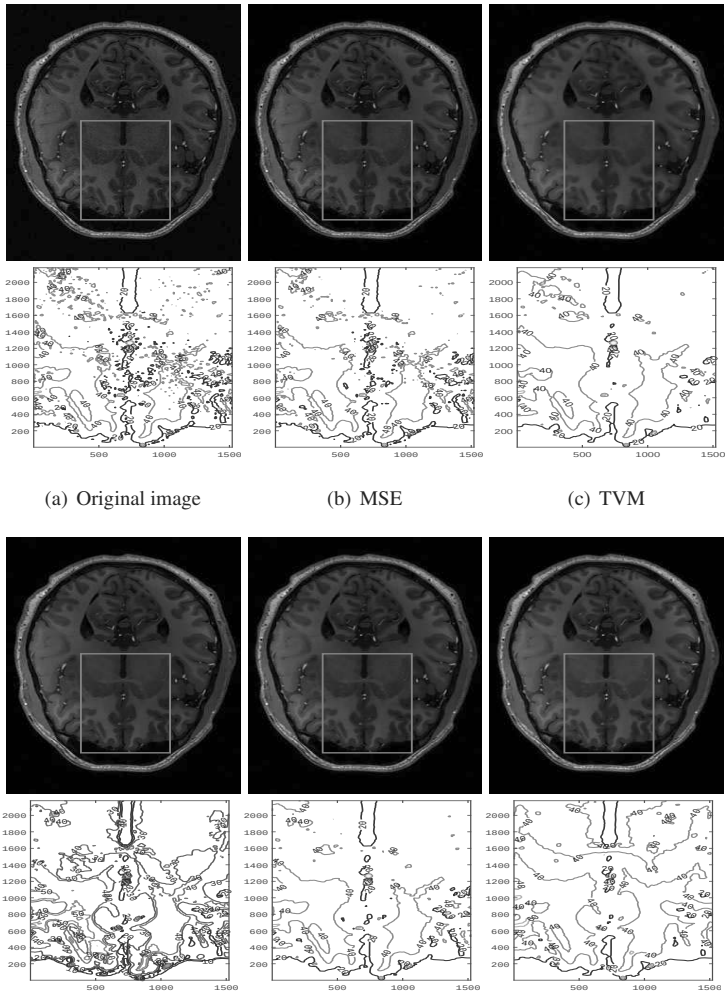

(a) Original image (b) MSE (c) TVM

(d) LGTV (e) CTV (f) NNC

Figure 9: Visual inspection for real 7T SENSE MRI, where $\lambda = 4$ for the TVM, $\gamma = 0.4$ for the CTV model and $\alpha = 0.4$, $\beta = 0.01$ for the NNC model.

geneous for the result obtained by the NNC model, especially the liver region (inside the red box). For Lumbar spine in Figure 11, the NNC model can not only gives more homogeneous result, but also recover the structures in the background.

In the end, we display both the bias corrected images and the estimated bias field for

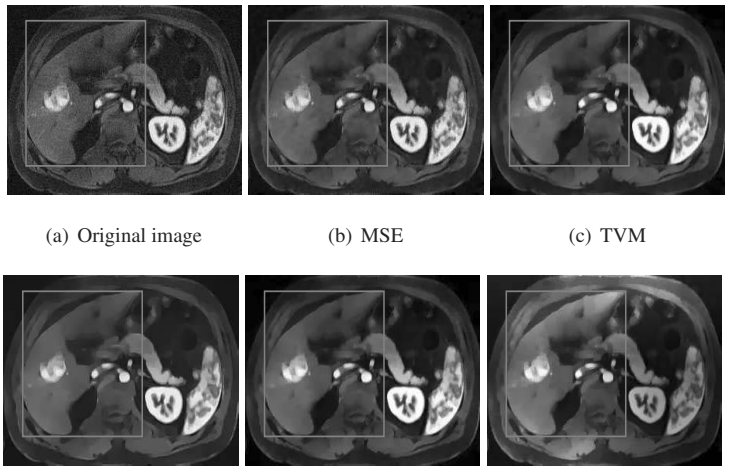

(a) Original image (b) MSE (c) TVM

(d) LGTV (e) CTV (f) NNC

Figure 10: Visual inspection for real Liver MRI, where $\lambda = 10$ for the TVM, $\gamma = 0.12$ for the CTV and $\alpha = 0.12$, $\beta = 0.0001$, $\gamma = 4$ for the NNC.

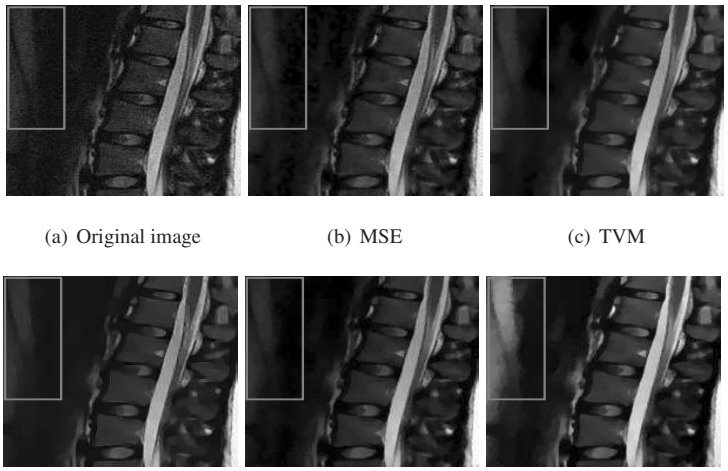

(a) Original image (b) MSE (c) TVM

(d) LGTV (e) CTV (f) NNC

Figure 11: Visual inspection for real Lumbar spine MRI. , where $\lambda = 10$ for the TVM, $\gamma = 0.12$ for the CTV and $\alpha = 0.12$, $\beta = 0.02$ for the NNC.

the real MRI data in Figure 12. Obviously, the intensities become more homogeneous for the bias corrected images and the estimated bias fields are spatially smooth as we assumed.

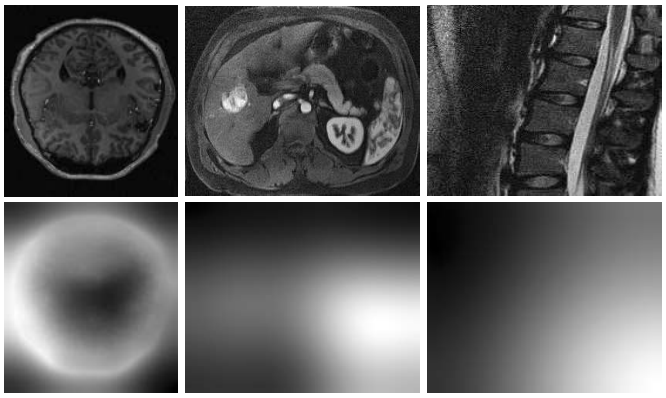

(a) 7T brain (b) Liver (c) Lumbar spine

Figure 12: The bias corrected images and estimated bias field of images in Figure 9, 10 and 11.

6. Conclusion

The Rician noise and intensity nonuniformity are two main factors leading to the degradation of MRI data. Although they may coexist in MRI data, current denoising methods can not deal with the intensity nonuniformity. In this paper, we proposed a novel restoration model for MRI data, which can handle the aforementioned problem. In our proposal, we modeled the noise-free image as a multiplication of the true intensity and the bias field, both of which are regularized based on suitable prior information. The numerical experiments show that the proposed method can achieve better results than the comparison methods and support different contrast type MRI data, i.e., PD-, T_1-, and T_2-weighted MRI data. Moreover, satisfactory results can be achieved on real MRI data. Future works includes to further improve the performance of NNC model by using more powerful regularization techniques, such as the total generalized variation, nonlocal total variation, etc.. Although we use experiments demonstrate that

the existence of intensity nonuniformity will lead to the underestimation of the Rician noise for both stationary and non-stationary approaches, there is still lack of quantitative evaluation of such effect. Thus, a possible and meaningful future work is to model the intensity nonuniformity in noise estimation for accurate image restoration.

Acknowledgments

The authors would like to thank Prof. Zeng Tieyong from Hong Kong Baptist University for providing us with MATLAB code of CTV [29]. We also thank Prof. Pang Zhifeng from Henan University for valuable discussion. The work is supported by the 1000 Talents Program for Young Scientists of China, NSFC 11701418, 11626250, and the Ministry of Science and Technology of China ("863" Program: 2015AA020101).

Appendix : Proof for Theorem 3.1

Proof. According to [31], the Rician data fidelity term is bounded below. Since the other terms in E are positive and proper, the infimum of $E(v,u,b)$ is finite. Let us pick a minimizing sequence $(v^n,u^n,b^n)\in BV(\Omega)\times BV(\Omega)\times H^1(\Omega)$. Then, there exists a constant $M>0$ such that $E(v^n,u^n,b^n)\leq M$. Thus, each term in $E(v^n,u^n,b^n)$ is bounded, i.e.,

$$\int_\Omega \frac{1}{2\sigma^2}(v^n)^2-\log I_0\big(\frac{v^n f}{\sigma^2}\big)dx \;\leq\; M,\;\; \int_\Omega (v^n-u^nb^n)^2dx \;\leq\; M,$$
$$\int_\Omega |\nabla v^n|dx \;\leq\; M,\;\; \int_\Omega |\nabla u^n|dx \;\leq\; M,\;\; \int_\Omega |\nabla b^n|^2dx \;\leq\; M,\;\; \int_\Omega |b^n|^2dx \;\leq\; M.$$

Since $v^n\in[0,255]$, $\|v^n\|_{L^1(\Omega)}=\int_\Omega |v^n|dx\leq 255|\Omega|$, where $|\Omega|$ is the area of Ω. Hence, $\|v^n\|_{BV(\Omega)}$ is uniformly bounded. By the compactness property of $BV(\Omega)$ and the relative compactness of $BV(\Omega)$ in $L^1(\Omega)$, up to a subsequence also denoted by $\{v^n\}$ after relabeling, there exists a function $v^*\in BV(\Omega)$ such that (a) $v^n\to v^*$ strongly in $L^1(\Omega)$, (b) $v^n\to v^*$ a.e. $x\in\Omega$, (c) $\nabla v^n \rightharpoonup \nabla v^*$ in the sense of measure. Due to the lower semi-continuity of the L^2 norm and total variation, it yields

$$\begin{aligned}\int_\Omega (v^*)^2dx \;&\leq\; \liminf_{n\to\infty}\int_\Omega (v^n)^2dx,\\ \int_\Omega |\nabla v^*|dx \;&\leq\; \liminf_{n\to\infty}\int_\Omega |\nabla v^n|dx.\end{aligned}\tag{21}$$

Since the sequence $\{v^n f\}$ is weakly convergent in $L^1(\Omega)$, it is equi-integrable. Thus, it follows from the estimate

$$\log I_0\big(\frac{v^n f}{\sigma^2}\big) \leq \frac{1}{\sigma^2} f|v^n|,$$

that the sequence $\Big\{ \log I_0\big(\frac{v_n f}{\sigma^2}\big) \Big\}$ is equi-integrable. Applying the compact embedding of $W^{1,1}(\Omega)$ into $L^1(\Omega)$, we will assume that

$$v^n(x) \to v^*(x), \qquad \text{pointwise a.e. in } \Omega,$$

which implies

$$\log I_0\big(\frac{v^n(x)f(x)}{\sigma^2}\big) \to \log I_0\big(\frac{v^*(x)f(x)}{\sigma^2}\big), \quad \text{a.e. in } \Omega. \tag{22}$$

Since $u^n \in [0, 255]$, $\|u^n\|_{L^1(\Omega)} = \int_\Omega |u^n| dx \leq 255|\Omega|$. Hence, $\|u^n\|_{BV(\Omega)}$ is uniformly bounded. Similarly, up to a subsequence also denoted by $\{u^n\}$ after relabeling, there exists a function $u^* \in BV(\Omega)$ such that (a) $u^n \to u^*$ strongly in $L^1(\Omega)$, (b) $u^n \to u^*$ a.e. $x \in \Omega$, (c) $\nabla u^n \rightharpoonup \nabla u^*$ in the sense of measure. The lower semi-continuity of the total variation yields

$$\int_\Omega |\nabla u^*| dx \leq \liminf_{n\to\infty} \int_\Omega |\nabla u^n| dx. \tag{23}$$

Without loss of generality, we can assume that $b^n_\Omega := \int_\Omega b^n dx = |\Omega|$. By the generalized Poincaré inequality in Ω, we have all n,

$$\|b^n\|_{L^2(\Omega)} = \|b^n - b^n_\Omega\|_{L^2(\Omega)} \leq C_1 \|\nabla b^n\|_{L^2(\Omega)} \leq C_2,$$

for some constant values C_1 and C_2. This implies that the sequence $\{b^n\}$ is bounded in $H^1(\Omega)$. By the L^2-weak compactness of the bounded H^1 sequence, there is a subsequence that is also denoted by $\{b^n\}$ after relabeling, and a function $b^* \in H^1(\Omega)$ satisfying (a) $b^n \to b^*$ strongly in $L^1(\Omega)$, (b) $b^n \to b^*$ a.e. $x \in \Omega$, (c) $b^n \rightharpoonup b^*$ weakly in $H^1(\Omega)$. By the lower semi-continuity of L^2 norm and H^1 norm, we have

$$\begin{aligned} \int_\Omega |b^*|^2 dx &\leq \liminf_{n\to\infty} \int_\Omega |b^n|^2 dx \\ \int_\Omega |\nabla b^*|^2 dx &\leq \liminf_{n\to\infty} \int_\Omega |\nabla b^n|^2 dx. \end{aligned} \tag{24}$$

Since $v^n \to v^*$ a.e. $x \in \Omega$, $u^n \to u^*$ a.e. $x \in \Omega$, $b^n \to b^*$ a.e. $x \in \Omega$, Fatou's lemma gives that

$$\int_\Omega (v^* - u^* b^*)^2 dx \;\leq\; \liminf_{n\to\infty} \int_\Omega (v^n - u^n b^n)^2 dx. \tag{25}$$

Combining inequalities from (21) to (25), we deduce that

$$E(v^*, u^*, b^*) \leq \liminf_{n\to\infty} E(v^n, u^n, b^n) = \inf E(v, u, b),$$

which indicates that (v^*, u^*, b^*) is a minimizer of problem (14). This completes the proof. □

References

[1] H. Gudbjartsson, S. Patz, The rician distribution of noisy mri data, Magnetic Resonance in Medicine 34 (6) (1995) 910–914. doi:10.1002/mrm.1910340618.

[2] B. Belaroussi, J. Milles, S. Carme, Y. M. Zhu, H. Benoit-Cattin, Intensity nonuniformity correction in mri: existing methods and their validation, Medical Image Analysis 10 (2) (2006) 234–246. doi:10.1016/j.media.2005.09.004.

[3] U. Vovk, F. Pernuš, B. Likar, A review of methods for correction of intensity inhomogeneity in mri, IEEE Transactions on Medical Imaging 26 (3) (2007) 405–421. doi:10.1109/TMI.2006.891486.

[4] D. L. Pham, J. L. Prince, Adaptive fuzzy segmentation of magnetic resonance images, IEEE Transactions on Medical Imaging 18 (9) (1999) 737–752. doi:10.1109/42.802752.

[5] S. Prima, N. Ayache, T. Barrick, N. Roberts, Maximum likelihood estimation of the bias field in mr brain images: Investigating different modelings of the imaging process, International Conference on Medical Image Computing and Computer Assisted Intervention (2001) 811–819doi:10.1007/3-540-45468-3.

[6] J. Ashburner, K. J. Friston, Unified segmentation, Neuroimage 26 (3) (2005) 839–851. doi:10.1016/j.neuroimage.2005.02.018.

[7] W. M. Wells, W. E. L. Grimson, R. Kikinis, F. A. Jolesz, Adaptive segmentation of mri data, IEEE Transactions on Medical Imaging 15 (4) (1996) 429–442. doi:10.1109/42.511747.

[8] K. Van Leemput, F. Maes, D. Vandermeulen, P. Suetens, Automated model-based bias field correction of mr images of the brain, IEEE Transactions on Medical Imaging 18 (10) (1999) 885–896. doi:10.1109/42.811268.

[9] D. L. Pham, J. L. Prince, An adaptive fuzzy c-means algorithm for image segmentation in the presence of intensity inhomogeneities, Pattern Recognition Letters 20 (1) (1999) 57–68. doi:10.1016/S0167-8655(98)00121-4.

[10] M. N. Ahmed, S. M. Yamany, N. Mohamed, A. A. Farag, T. Moriarty, A modified fuzzy c-means algorithm for bias field estimation and segmentation of mri data, IEEE Transactions on Medical Imaging 21 (3) (2002) 193–199. doi:10.1109/42.996338.

[11] C. Li, R. Huang, Z. Ding, J. C. Gatenby, D. N. Metaxas, J. C. Gore, A level set method for image segmentation in the presence of intensity inhomogeneities with application to mri, IEEE Transactions on Image Processing 20 (7) (2011) 2007–2016. doi:10.1109/TIP.2011.2146190.

[12] C. Li, J. C. Gore, C. Davatzikos, Multiplicative intrinsic component optimization (mico) for mri bias field estimation and tissue segmentation, Magnetic Resonance Imaging 32 (7) (2014) 913–923. doi:10.1016/j.mri.2014.03.010.

[13] J. G. Sled, A. P. Zijdenbos, A. C. Evans, A nonparametric method for automatic correction of intensity nonuniformity in mri data, IEEE Transactions on Medical Imaging 17 (1) (1998) 87–97. doi:10.1109/42.668698.

[14] N. J. Tustison, B. B. Avants, P. Cook, Y. Zheng, A. Egan, P. Yushkevich, J. C. Gee, et al., N4itk: improved n3 bias correction, IEEE Transactions on Medical Imaging 29 (6) (2010) 1310–1320. doi:10.1109/TMI.2010.2046908.

[15] J. Ashburner, K. J. Friston, Voxel-based morphometry–the methods, Neuroimage 11 (6) (2000) 805–821. doi:10.1006/nimg.2000.0582.

[16] U. Vovk, F. B. Pernus, Mri intensity inhomogeneity correction by combining intensity and spatial information, Physics in Medicine and Biology 49 (17) (2004) 4119–4133. doi:10.1088/0031-9155/49/17/020.

[17] J. V. Manjón, J. J. Lull, J. Carbonell-Caballero, G. García-Martí, L. Martí-Bonmatí, M. Robles, A nonparametric mri inhomogeneity correction method, Medical Image Analysis 11 (4) (2007) 336–345. doi:10.1016/j.media.2007.03.001.

[18] H. Chang, W. Huang, C. Wu, S. Huang, C. Guan, S. Sekar, K. Bhakoo, Y. Duan, A new variational method for bias correction and its applications to rodent brain extraction, IEEE Transactions on Medical Imaging 36 (3) (2017) 721–733. doi:10.1109/TMI.2016.2636026.

[19] A. Den Dekker, J. Sijbers, Data distributions in magnetic resonance images: A review, Physica Medica 30 (7) (2014) 725–741. doi:10.1016/j.ejmp.2014.05.002.

[20] P. Bao, L. Zhang, Noise reduction for magnetic resonance images via adaptive multiscale products thresholding, IEEE Transactions on Medical Imaging 22 (9) (2003) 1089–1099. doi:10.1109/TMI.2003.816958.

[21] R. M. Henkelman, Erratum: Measurement of signal intensities in the presence of noise in mr images [med. phys. 12, 232 (1985)], Medical physics 13 (4) (1986) 544–544. doi:10.1118/1.595860.

[22] G. Gerig, O. Kubler, R. Kikinis, F. A. Jolesz, Nonlinear anisotropic filtering of mri data, IEEE Transactions on Medical Imaging 11 (2) (1992) 221–232. doi:10.1109/42.141646.

[23] S. Aja-Fernández, C. Alberola-López, C.-F. Westin, Noise and signal estimation in magnitude mri and rician distributed images: a lmmse approach, IEEE Trans-

actions on Image Processing 17 (8) (2008) 1383–1398. doi:10.1109/TIP.2008.925382.

[24] K. Krissian, S. Aja-Fernández, Noise-driven anisotropic diffusion filtering of mri, IEEE Transactions on Image Processing 18 (10) (2009) 2265–2274. doi:10.1109/TIP.2009.2025553.

[25] P. V. Sudeep, P. Palanisamy, C. Kesavadas, J. Rajan, Nonlocal linear minimum mean square error methods for denoising mri, Biomedical Signal Processing and Control 20 (2015) 125–134. doi:10.1016/j.bspc.2015.04.015.

[26] R. D. Nowak, Wavelet-based rician noise removal for magnetic resonance imaging, IEEE Transactions on Image Processing 8 (10) (1999) 1408–1419. doi:10.1109/83.791966.

[27] P. Getreuer, M. Tong, L. A. Vese, A variational model for the restoration of mr images corrupted by blur and rician noise, in: International Symposium on Visual Computing, Springer, 2011, pp. 686–698. doi:10.1007/978-3-642-24028-7_63.

[28] R. W. Liu, L. Shi, W. Huang, J. Xu, S. C. H. Yu, D. Wang, Generalized total variation-based mri rician denoising model with spatially adaptive regularization parameters, Magnetic Resonance Imaging 32 (6) (2014) 702–720. doi:10.1016/j.mri.2014.03.004.

[29] L. Chen, T. Zeng, A convex variational model for restoring blurred images with large rician noise, Journal of Mathematical Imaging and Vision 53 (1) (2015) 92–111. doi:10.1007/s10851-014-0551-y.

[30] M. Kang, M. Kang, M. Jung, Nonconvex higher-order regularization based rician noise removal with spatially adaptive parameters, Journal of Visual Communication and Image Representation 32 (2015) 180–193. doi:10.1016/j.jvcir.2015.08.006.

[31] A. Martín, E. Schiavi, S. S. de León, On 1-laplacian elliptic equations modeling magnetic resonance image rician denoising, Journal of Mathematical Imaging and Vision 57 (2) (2017) 202–224. doi:10.1007/s10851-016-0675-3.

[32] A. Chambolle, T. Pock, A first-order primal-dual algorithm for convex problems with applications to imaging, Journal of Mathematical Imaging and Vision 40 (1) (2011) 120–145. doi:10.1007/s10851-010-0251-1.

[33] L. I. Rudin, S. Osher, E. Fatemi, Nonlinear total variation based noise removal algorithms, Physica D: Nonlinear Phenomena 60 (1-4) (1992) 259–268. doi:10.1016/0167-2789(92)90242-F.

[34] A. Chambolle, An algorithm for total variation minimization and applications, Journal of Mathematical Imaging and Vision 20 (1–2) (2004) 89–97. doi:10.1023/B:JMIV.0000011325.36760.1e.

[35] G. Aubert, A. Jean-Francois, A variational approach to removing multiplicative noise, SIAM Journal on Applied Mathematics 68 (4) (2008) 925–946. doi:10.1137/060671814.

[36] D. Mumford, J. Shah, Optimal approximations by piecewise smooth functions and associated variational problems, Communications on Pure and Applied Mathematics 42 (5) (1989) 577–685. doi:10.1002/cpa.3160420503.

[37] J.-F. Aujol, G. Gilboa, T. Chan, S. Osher, Structure-texture image decomposition-modeling, algorithms, and parameter selection, International Journal of Computer Vision 67 (1) (2006) 111–136. doi:10.1007/s11263-006-4331-z.

[38] Y.-M. Huang, M. K. Ng, Y.-W. Wen, A new total variation method for multiplicative noise removal, SIAM Journal on Imaging Sciences 2 (1) (2009) 20–40. doi:10.1137/080712593.

[39] R. Kimmel, M. Elad, D. Shaked, R. Keshet, I. Sobel, A variational framework for retinex, International Journal of Computer Vision 52 (1) (2003) 7–23. doi:10.1023/A:1022314423998.

[40] D. L. Collins, A. P. Zijdenbos, V. Kollokian, J. G. Sled, N. J. Kabani, C. J. Holmes, A. C. Evans, Design and construction of a realistic digital brain phantom, IEEE Transactions on Medical Imaging 17 (3) (1998) 463–468. doi:10.1109/42.712135.

[41] Z. Wang, A. C. Bovik, H. R. Sheikh, E. P. Simoncelli, Image quality assessment: from error visibility to structural similarity, IEEE Transactions on Image Processing 13 (4) (2004) 600–612. doi:10.1109/TIP.2003.819861.

[42] T. Pieciak, S. Aja-Fernandez, G. Vegas-Sánchez-Ferrero, Non-stationary rician noise estimation in parallel mri using a single image: a variance-stabilizing approach, IEEE Transactions on Pattern Analysis and Machine Intelligence 39 (10) (2017) 2015–2029. doi:10.1109/TPAMI.2016.2625789.

[43] P. Coupé, J. V. Manjón, E. Gedamu, D. Arnold, M. Robles, D. L. Collins, Robust rician noise estimation for mr images, Medical Image Analysis 14 (4) (2010) 483–493. doi:10.1016/j.media.2010.03.001.

[44] S. Aja-Fernández, T. Pie, G. Vegas-Sánchez-Ferrero, et al., Spatially variant noise estimation in mri: A homomorphic approach, Medical Image Analysis 20 (1) (2015) 184–197.